Antigen-presenting microrobots program CAR-T cell function

Bo Zhang[1,*], Yan-Ruide Li[1,2,*], Shubing Wang[1], Junyu Nan[3], Xinyuan Shen[1,2], Jennifer Soto[1], Youcheng Yang[1], Hao Zhou[3], Haochen Nan[1], Yuning Chen[1,2], Zeyang Liu[1], Chun-Hsien Chen[1], Keyue Shen[3], Lili Yang[1,2,4,5,6,7,8,§], Song Li[1,4,5,9,§]

Author Affiliation:

[1]Department of Bioengineering, University of California, Los Angeles, Los Angeles, CA 90095, USA

[2]Department of Microbiology, Immunology & Molecular Genetics, University of California, Los Angeles, Los Angeles, CA 90095, USA

[3]Department of Biomedical engineering, University of Southern California, Los Angeles, CA 90089, USA

[4]The Eli and Edythe Broad Center of Regenerative Medicine and Stem Cell Research, University of California, Los Angeles, Los Angeles, CA 90095, USA

[5]Jonsson Comprehensive Cancer Centre, University of California, Los Angeles, Los Angeles, CA 90095, USA

[6]Molecular Biology Institute, University of California, Los Angeles, Los Angeles, CA 90095, USA

[7]Parker Institute for Cancer Immunotherapy, University of California, Los Angeles, Los Angeles, CA 90095, USA

[8]Goodman-Luskin Microbiome Center, University of California, Los Angeles, Los Angeles, CA 90095, USA

[9]California NanoSystems Institute, University of California, Los Angeles, Los Angeles, CA, 90095, USA

*These authors contributed equally: Bo Zhang, Yan-Ruide Li.

[§]Corresponding author. Email: liliyang@ucla.edu (L.Y.), and songli@ucla.edu (S.L.).

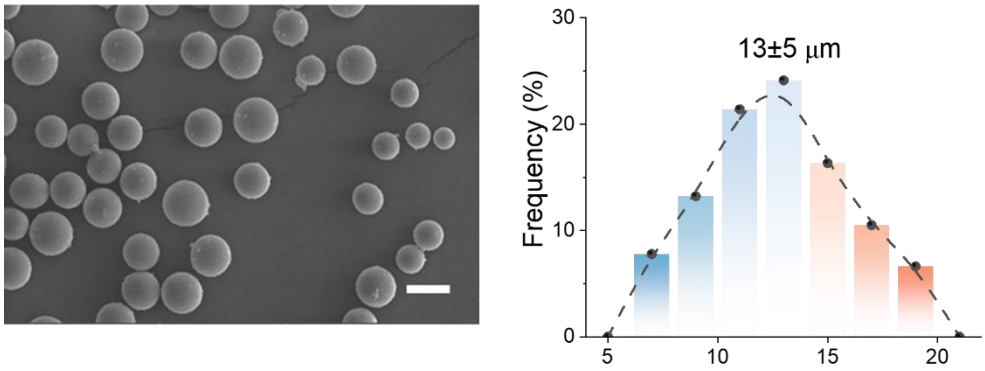


Figure S1. Morphology of magnesium particles by SEM and size distribution (number of images, n=8). Scale bar: 20 μm.

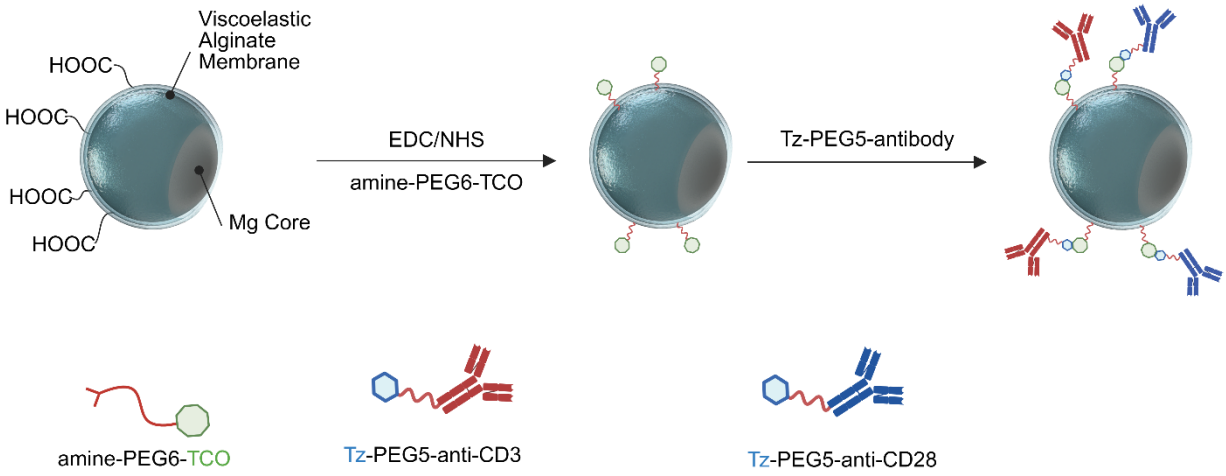


Figure S2. Surface functionalization of Cytobots via bio-orthogonal click chemistry. Carboxylated CytoBot surfaces were first activated with EDC/NHS and reacted with amine-PEG6-TCO to introduce strained alkenes. Tetrazine-PEG5-conjugated anti-CD3 and anti-CD28 antibodies were subsequently attached through rapid TCO–Tz click chemistry, yielding dual-antibody functionalized Cytobots for T-cell activation.

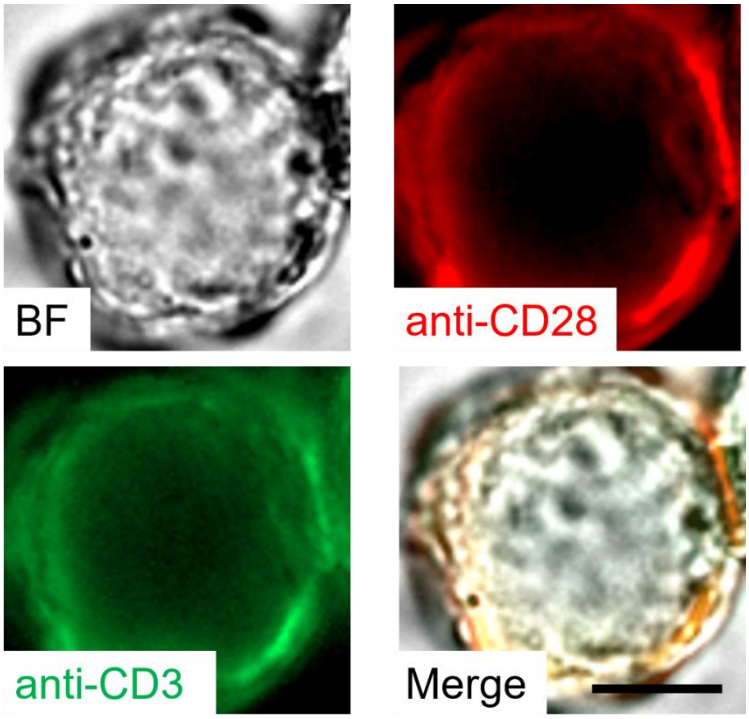


Figure S3. Fluorescence imaging demonstrating the morphological and antigenic biomimicry of the CytoBot top. A uniform surface distribution of anti-CD3 and anti-CD28 complexes on the CytoBots was observed. Scale bar: 5 μm.

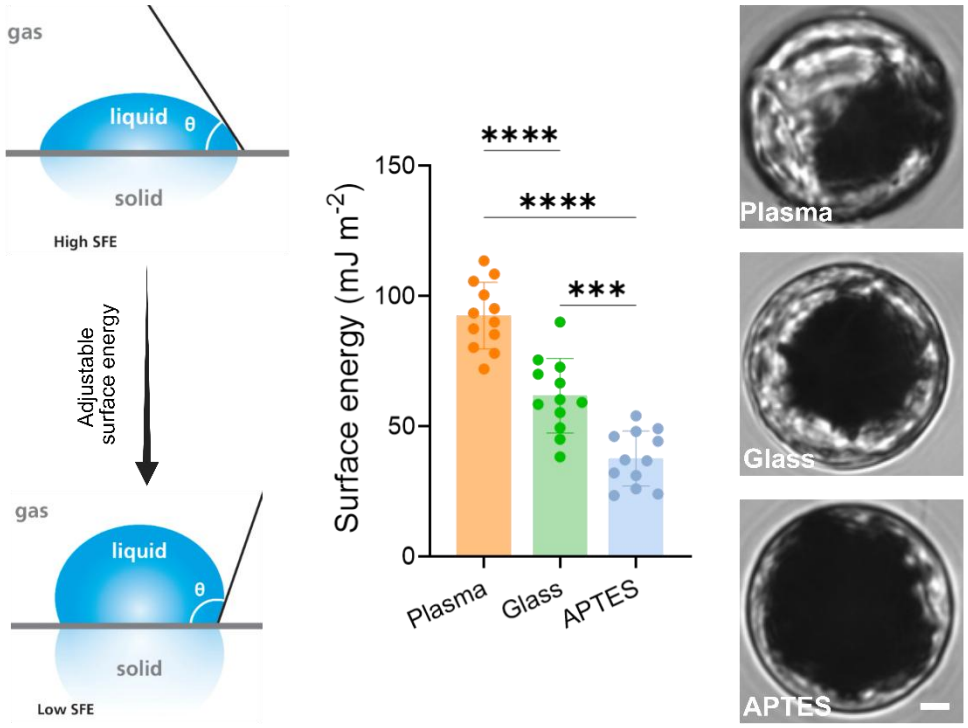


Figure S4. Optimization of CytoBot reactive-window fabrication by surface energy regulation. Schematic illustration of the fabrication strategy. Substrates with different surface free energies (SFEs) were used to regulate liquid wettability during protective-layer formation, thereby controlling the size of the exposed reactive window. Surface free energy of plasma-treated glass, untreated glass, and APTES-modified glass. Representative optical images of the resulting CytoBots prepared on each substrate are shown on the right. Different surface treatments produced CytoBots with distinct reactive-window sizes and fabrication stability.

For statistical analysis, multiple comparisons were performed by using ordinary two-way ANOVA, followed by Tukey's multiple comparisons test. P values less than 0.05 were considered significant. *P < 0.05; **P < 0.01; ***P < 0.001; ****P < 0.0001. Data are presented as mean ± SEM. This statistical labeling is used for all figures in Supporting Information.

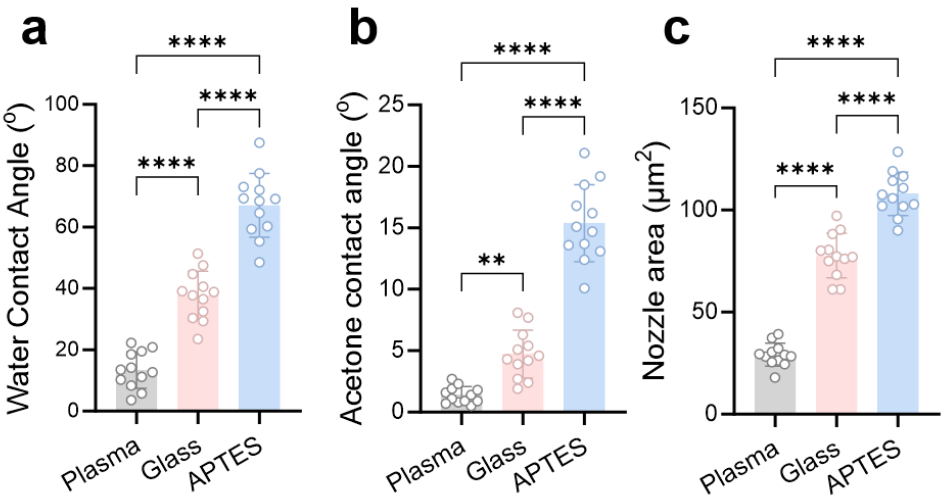


Figure S5. Optimization of CytoBot reactive-window fabrication by substrate surface energy.
(a) Water contact angles of plasma-treated, untreated glass, and APTES-modified substrates.
(b) Acetone contact angles of the corresponding substrates, reflecting differences in surface wettability.
(c) Quantification of the reactive-window area of CytoBots fabricated on different substrates. Regulating substrate surface energy altered liquid spreading during protective-layer formation, thereby controlling the size of the exposed Mg reactive window for subsequent propulsion.

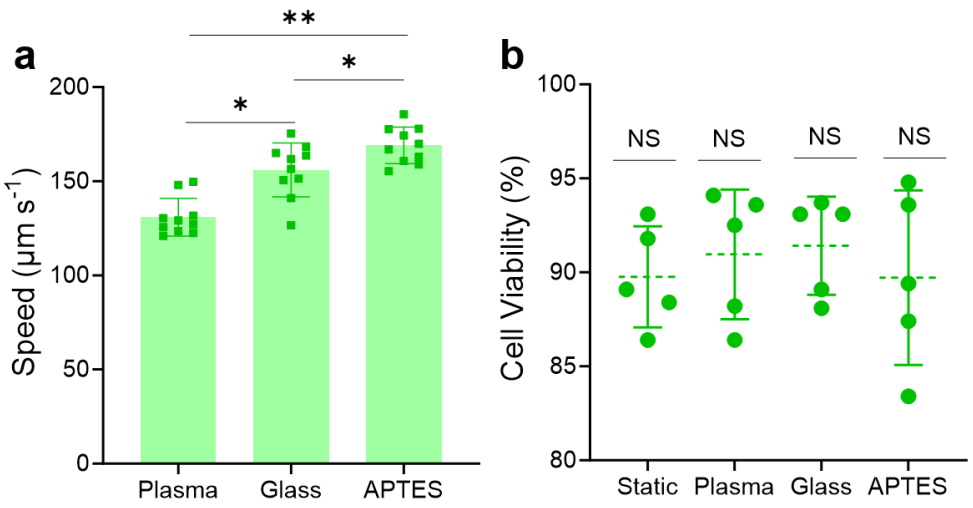


Figure S6. Optimization of CytoBot propulsion performance.

(a) Propulsion speed of CytoBots fabricated on plasma-treated, untreated glass, and APTES-modified substrates. Modulating substrate surface energy during fabrication influenced the exposed reactive-window geometry and consequently the propulsion velocity.

(b) Cell viability after incubation with CytoBots fabricated under different conditions, demonstrating comparable cytocompatibility across all fabrication strategies.

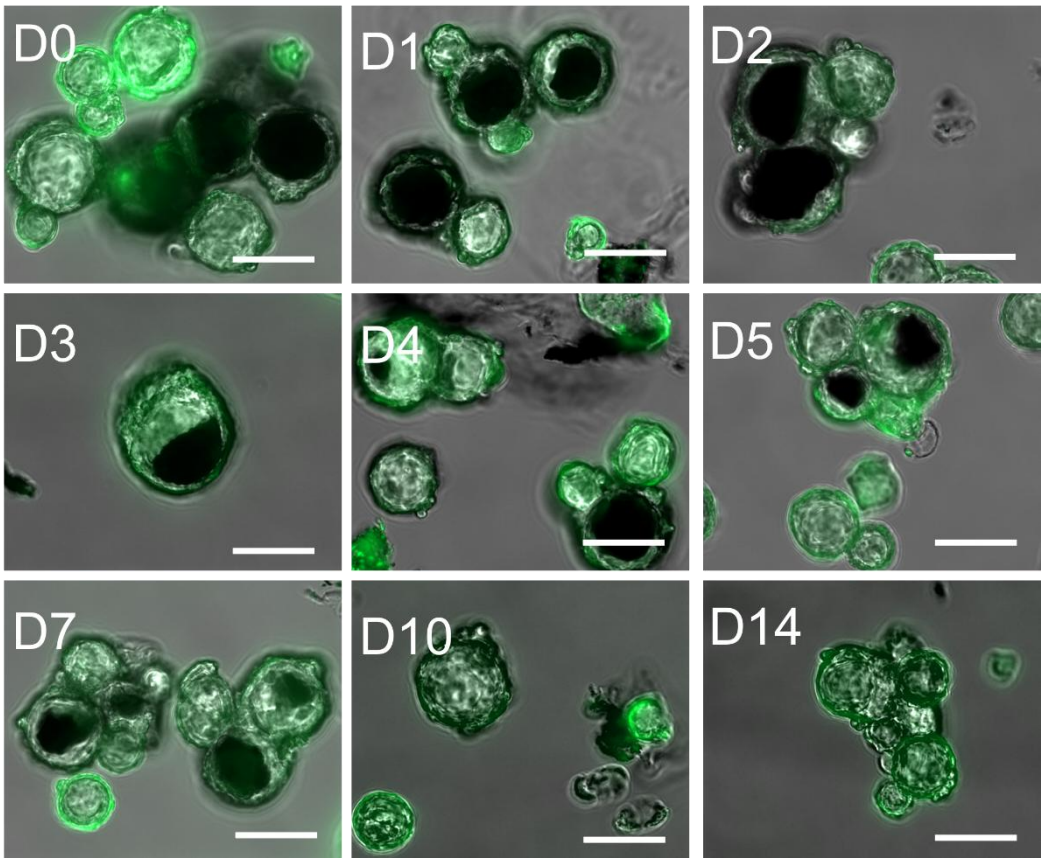


Figure S7. Degradation process of CytoBot in PBS over 14 days. Scale bar: 20 μm.

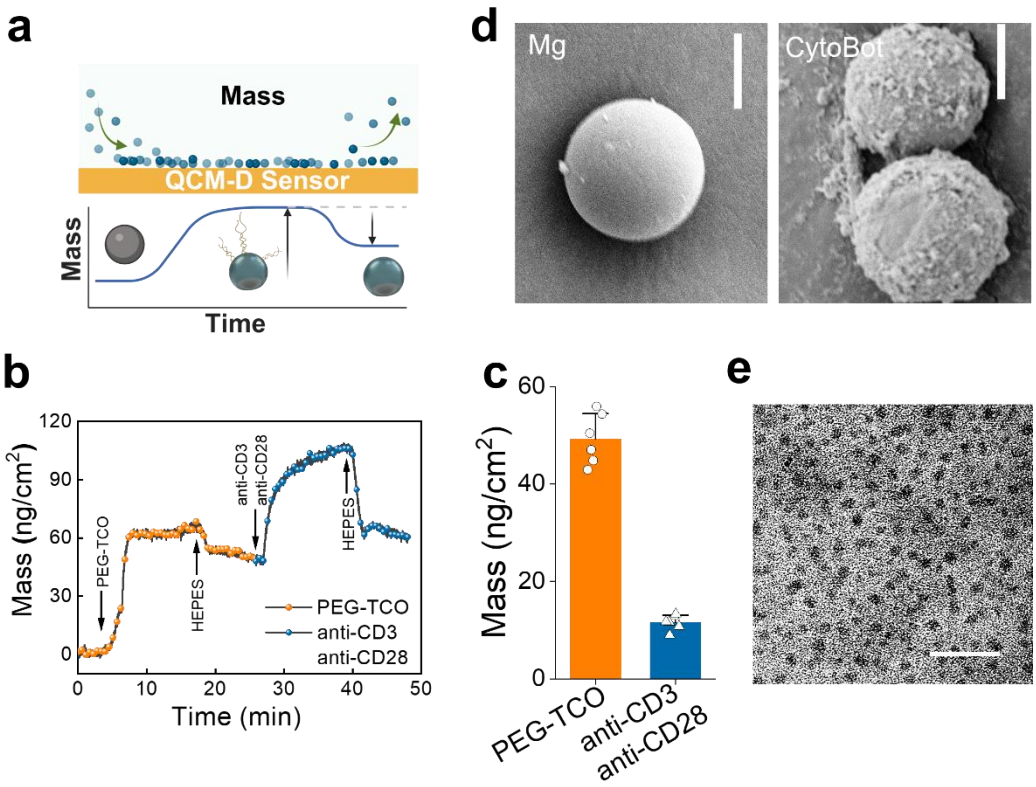


Figure S8. QCM-based quantification of CytoBot surface functionalization and morphological characterization.

(a) Schematic illustration of QCM-based quantification of PEG-TCO and antibody conjugation on the CytoBot surface.

(b) A clear mass increase was detected following sequential PEG-TCO deposition and subsequent antibody conjugation (e.g., anti-CD3 or anti-CD28), confirming successful surface functionalization.

(c) Quantitative analysis of surface mass change corresponding to PEG-TCO modification and antibody conjugation.

(d) Representative morphologies of CytoBots and bare magnesium particles. Scale bar: 5 μm.

(e) A TEM image negatively stained with uranyl acetate showing the CytoBot-linked protein. Scale bar: 100 nm.

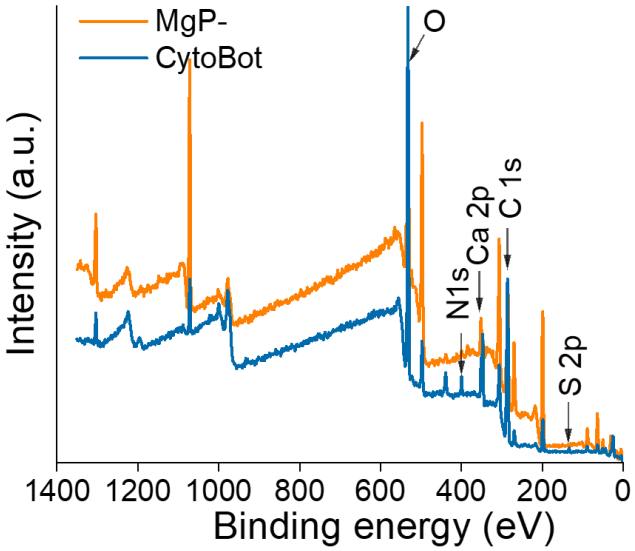


Figure S9. XPS analysis of surface elemental composition of CytoBot and MgP samples. Distinct differences in S 2p and N 1s peak intensities between the two samples indicate successful stepwise surface functionalization and biointerface formation.

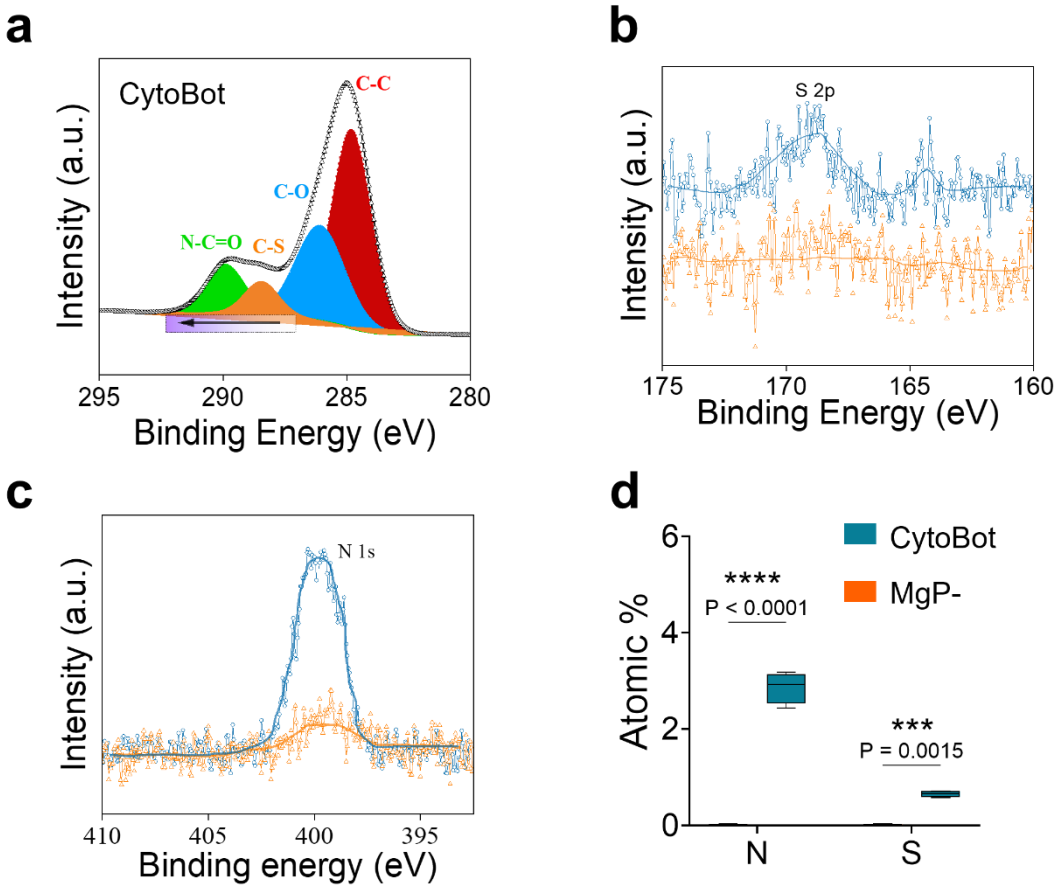


Figure S10. Characterization of CytoBot surface chemistry and elemental composition.
(a) Surface chemistry and topographical characterization of the coating. High-resolution C 1s spectrum of the CytoBot group showing characteristic deconvoluted peaks corresponding to C–C/C=C, C–O, N–C=O, and C–S, confirming successful incorporation of polysaccharide–polyphenol components.
(b) High-resolution S 2p spectrum showing distinct sulfur-containing chemical states associated with anti-CD3 and anti-CD28.
(c) High-resolution N 1s spectrum highlighting the increased amide/amine-related signals on the CytoBot surface.
(d) Quantitative comparison of N and S elemental ratios between CytoBot and MgP- groups, indicating enriched nitrogen- and sulfur-containing functionalities following CytoBot assembly.

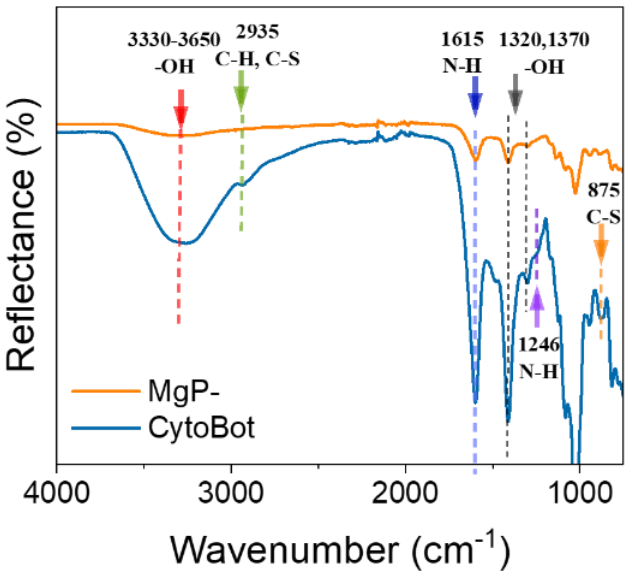


Figure S11. **ATR-FTIR spectra of the microspheres further reveal the functional groups present on the surface.** The appearance of specific absorption bands, such as –OH, –C-S, –NH, provides additional evidence of chemical functionalization.

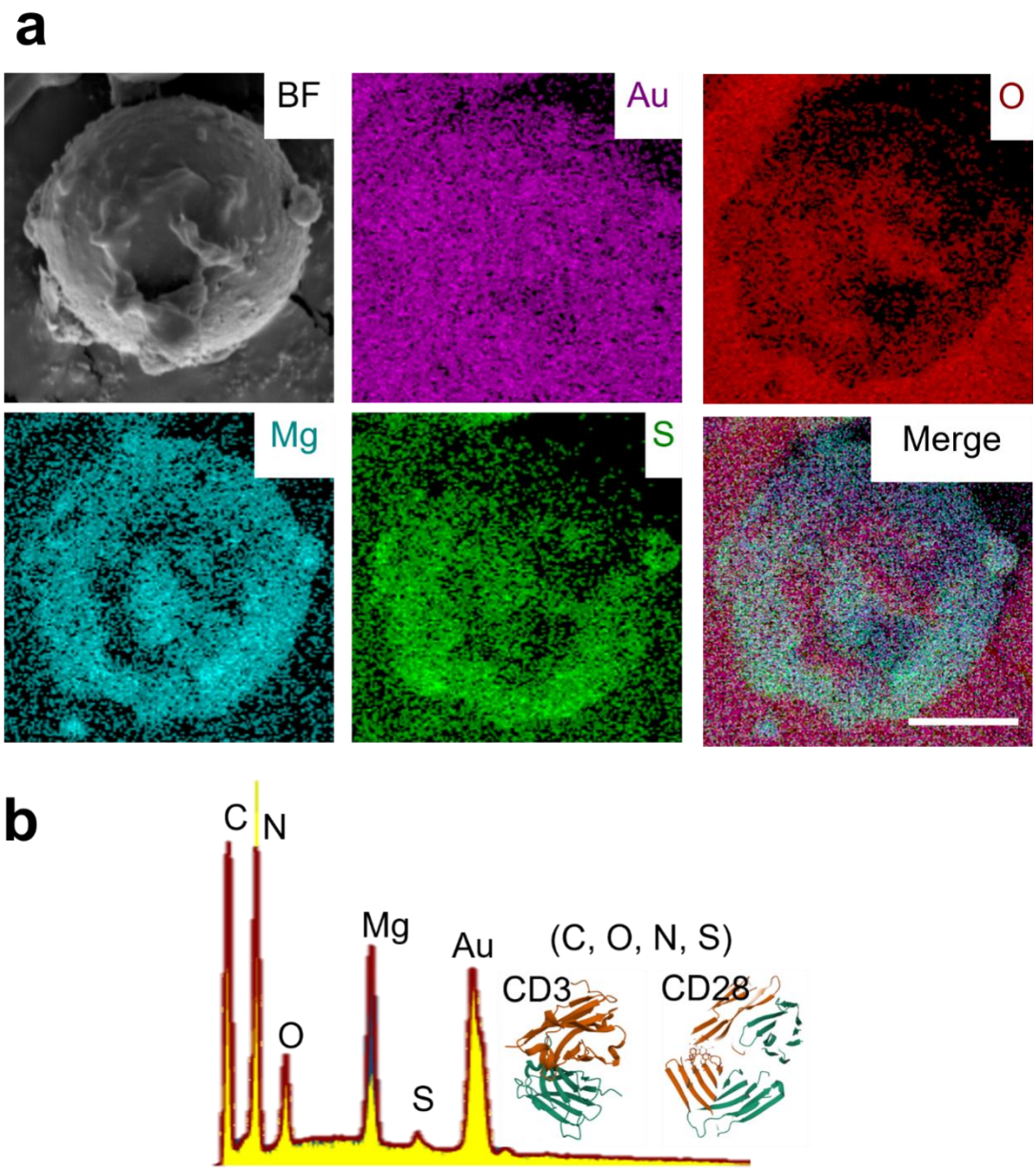


Figure S12. SEM–EDS characterization and elemental composition analysis of CytoBots.
(a) Representative SEM image and corresponding EDS elemental maps of a CytoBot, showing the distribution of Au, Mg, O, and S. Merged image illustrates the elemental composition of the particle. Scale bar: 5 μm.
(b) The EDS spectrum reveals Au, Mg, O, S, C, and N signals, consistent with the elemental composition of the functionalized CytoBot surface.

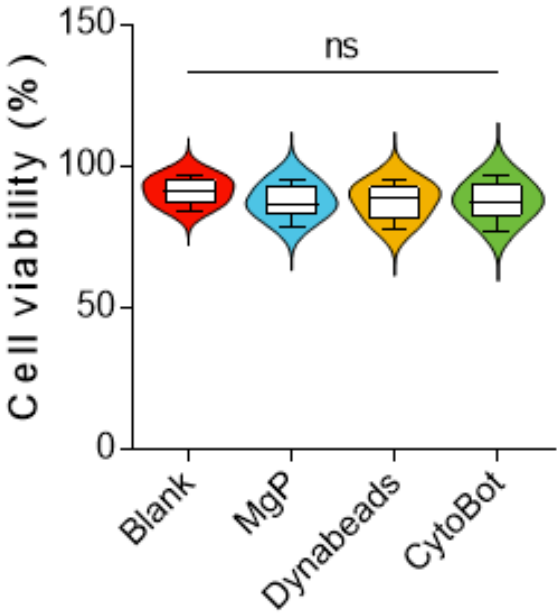


Figure S13. Quantification of T cell viability at 24 hours after co-culture with different beads, assessed by using a LIVE/DEAD staining. ns: no significant difference.

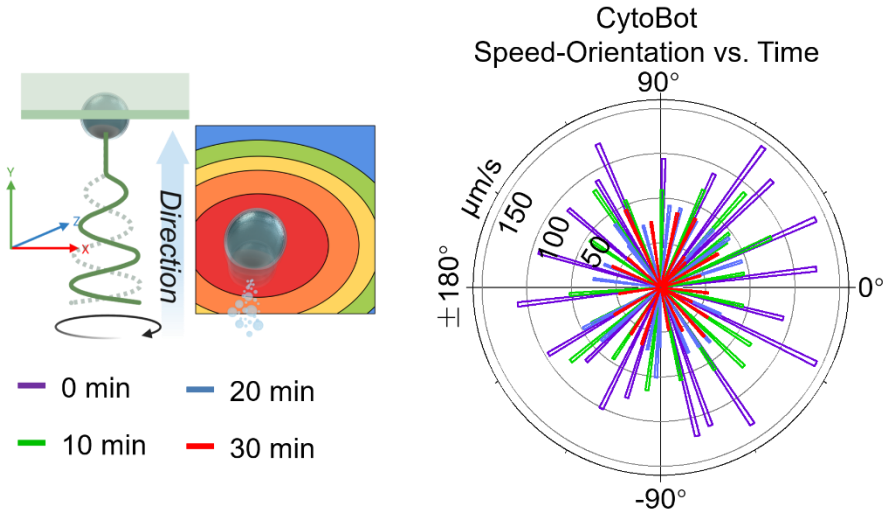


Figure S14. Locomotion of CytoBots in cell culture medium and time-dependent distribution of the speed and direction of CytoBot locomotion.

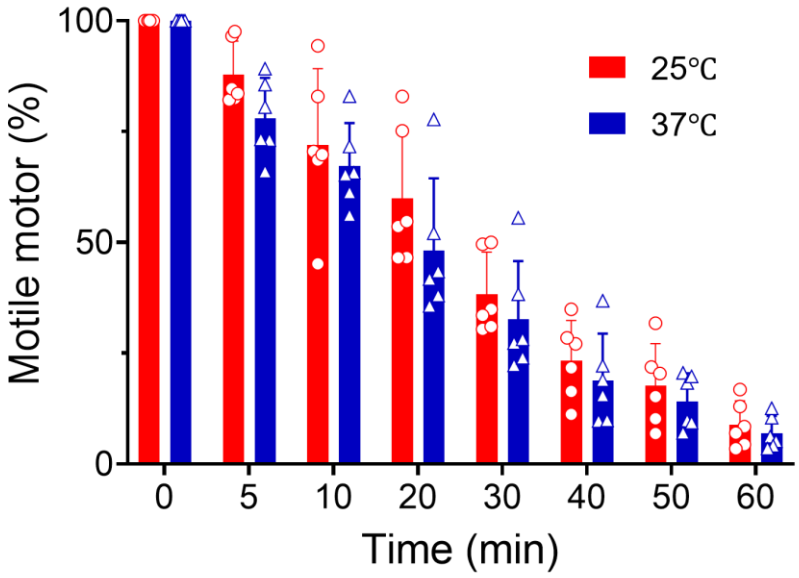


Figure S15. Time-dependent variations in CytoBot motility in T cell culture medium.

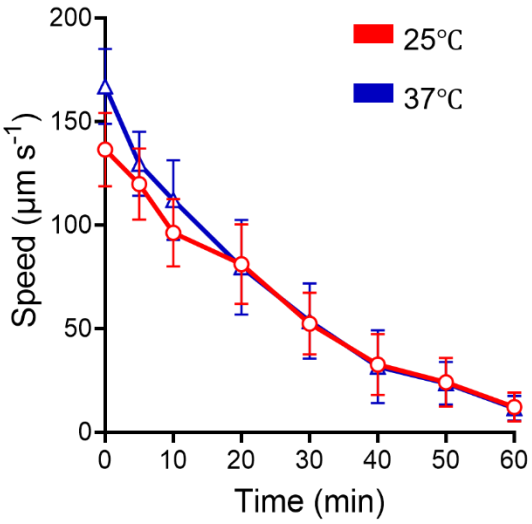


Figure S16. Comparison of CytoBot speeds in RPMI-1640 T cell culture medium at room temperature (25 °C) and body temperature (37 °C) (red and blue curves, respectively; n = 6).

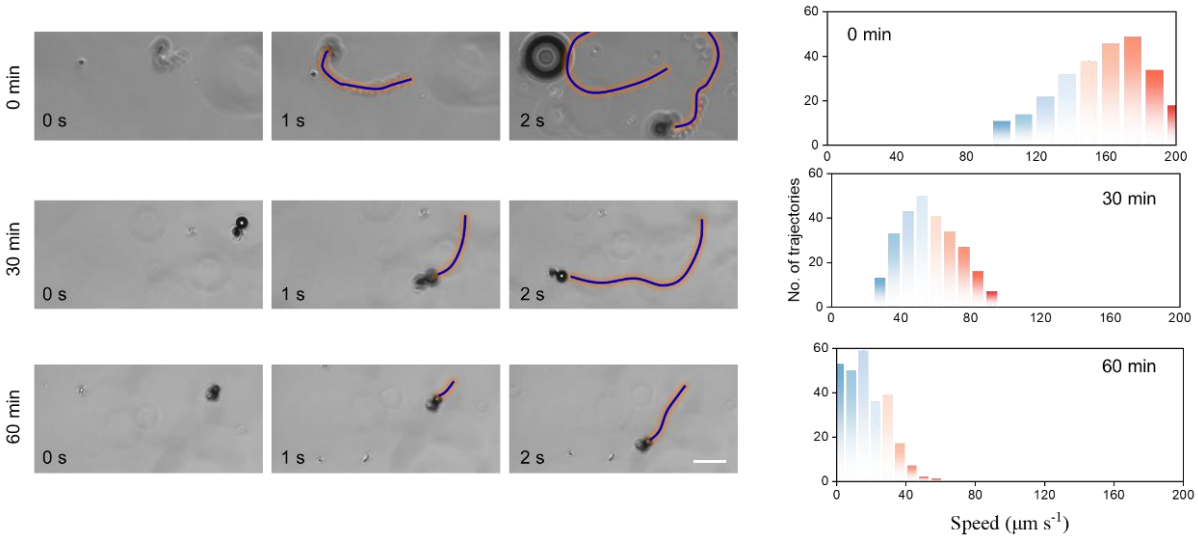


Figure S17. Representative tracking trajectories at 0, 1, and 2 seconds, and mean speed distribution of CytoBot in RPMI-1640 medium at 37℃ after 0 min, 30 min, and 60 min. Scale bar, 30 μm.

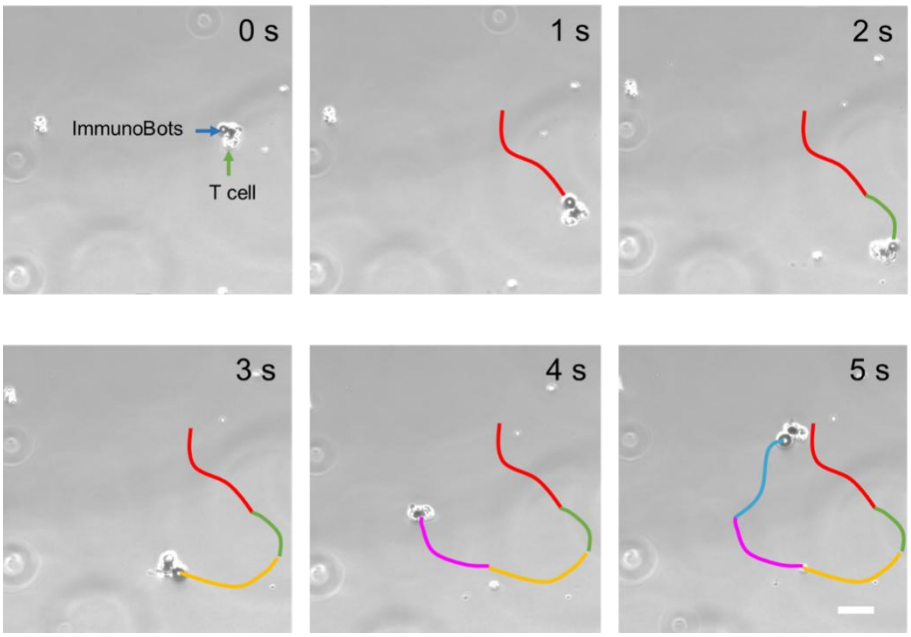


Figure S18. Representative tracking trajectories at 0 to 5 seconds. Scale bar, 20 μm.

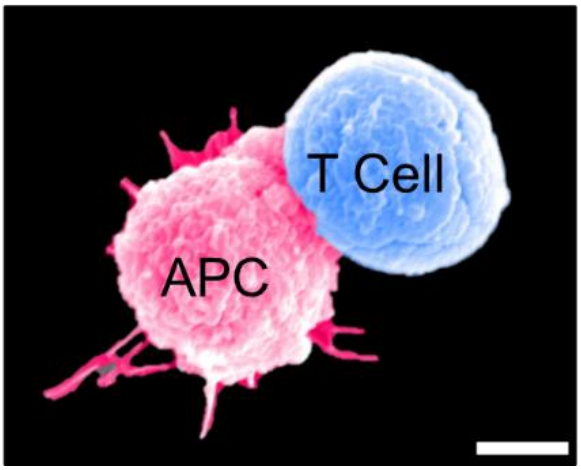


Figure S19. SEM images showing T cells interacting with a dendritic cell (APC) after 2 hours of co-culture. Scale bar: 5 μm.

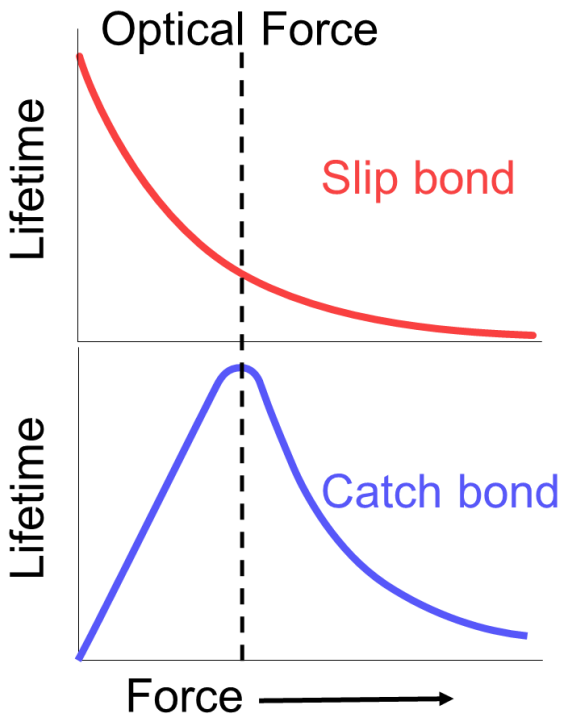


Figure S20. Schematic illustration of force-dependent slip-bond and catch-bond behavior. Slip bonds exhibit a monotonic decrease in bond lifetime with increasing applied force, whereas catch bonds display an initial increase in bond lifetime under moderate mechanical loading, followed by a decrease at higher forces. The dashed line schematically indicates an intermediate force regime associated with catch-bond stabilization. The curves are conceptual representations rather than experimental measurements.

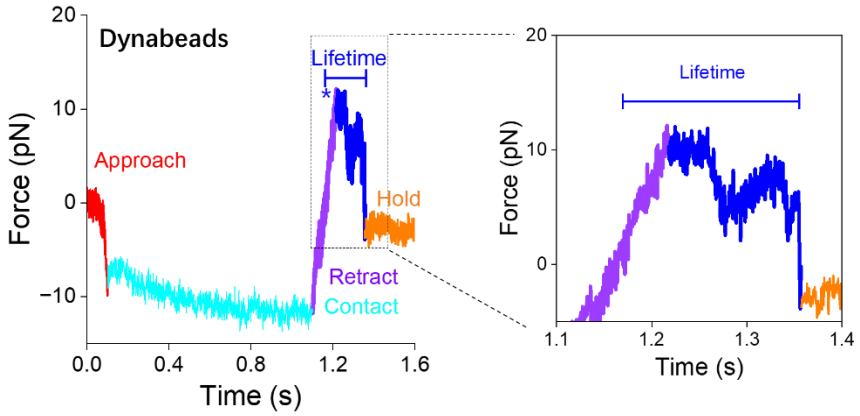


Figure S21. Representative force traces from microsphere measurement cycles depicting adhesion events that resisted the applied force ramp and maintained a preset force until bond rupture (highlighted by a blue star). The contact duration between the microsphere and the cell was controlled at 1 second.

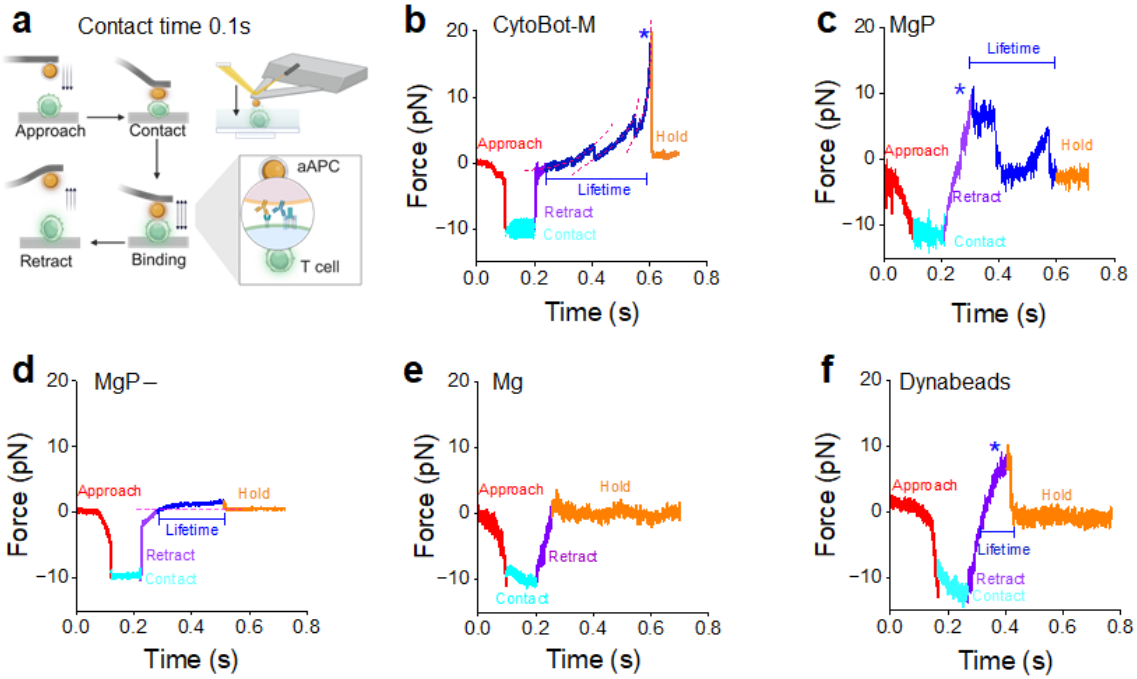


Figure S22. Bond formation between CytoBot-M and T cells.
Representative force traces from microspheres measurement cycles depicting adhesion events that resisted the applied force ramp and maintained a preset force until bond rupture (highlighted by a blue star). **(a)** The contact duration between the microsphere and the cell was controlled at 0.1 s. Measurements were performed at a setpoint force of 10 pN with contact times of 0.1 s. (**b**) CytoBot-M was operated at a locomotion speed of 50 µm/s, while (**c**) MgP, (**d**) MgP-, (**e**) Mg and (**f**) Dynabeads were tested at 0.2 µm/s.

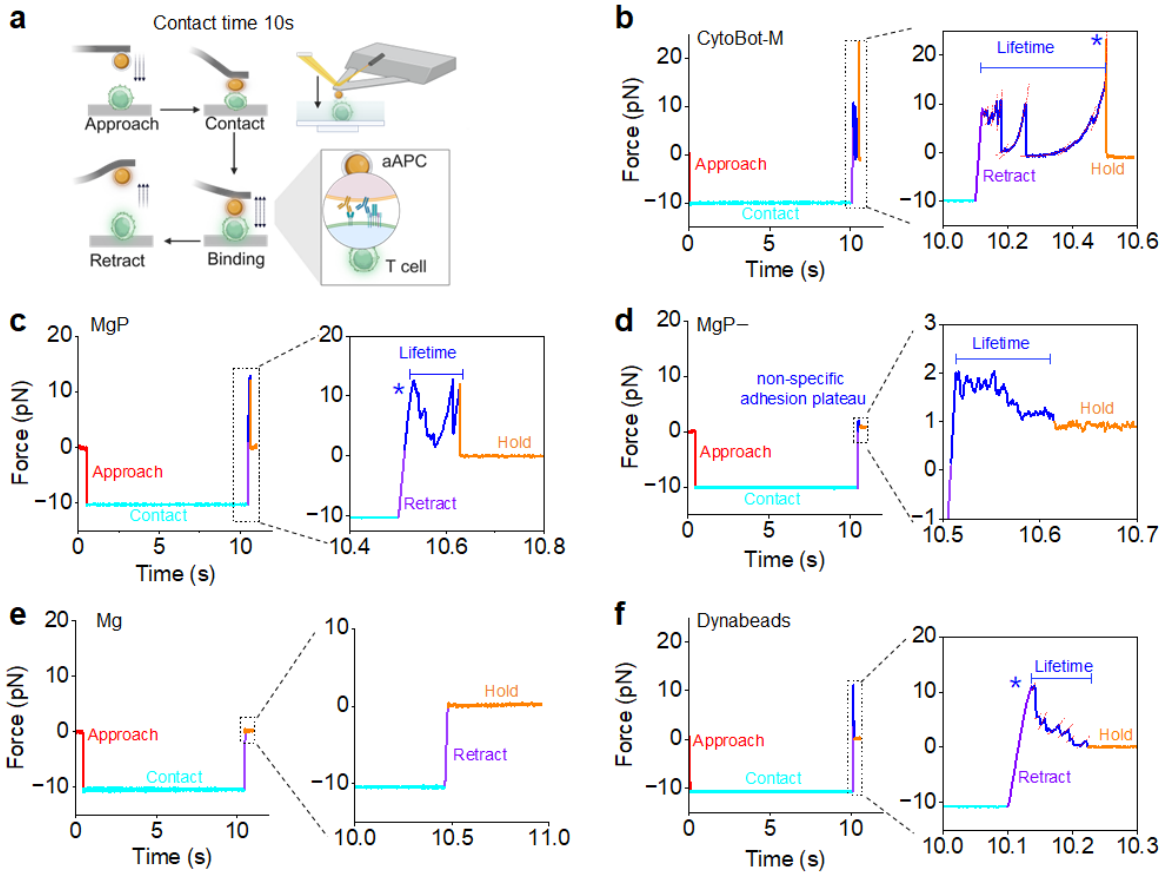


Figure S23. Bond formation between CytoBot-M and T cells.
Representative force traces from microspheres measurement cycles depicting adhesion events that resisted the applied force ramp and maintained a preset force until bond rupture (highlighted by a blue star). (**a**) The contact duration between the microsphere and the cell was controlled at 10 s. Measurements were performed at a setpoint force of 10 pN with contact times of 10 s. (**b**) CytoBot-M was operated at a locomotion speed of 50 µm/s, while (**c**) MgP, (**d**) MgP-, (**e**) Mg and (**f**) Dynabeads were tested at 0.2 µm/s.

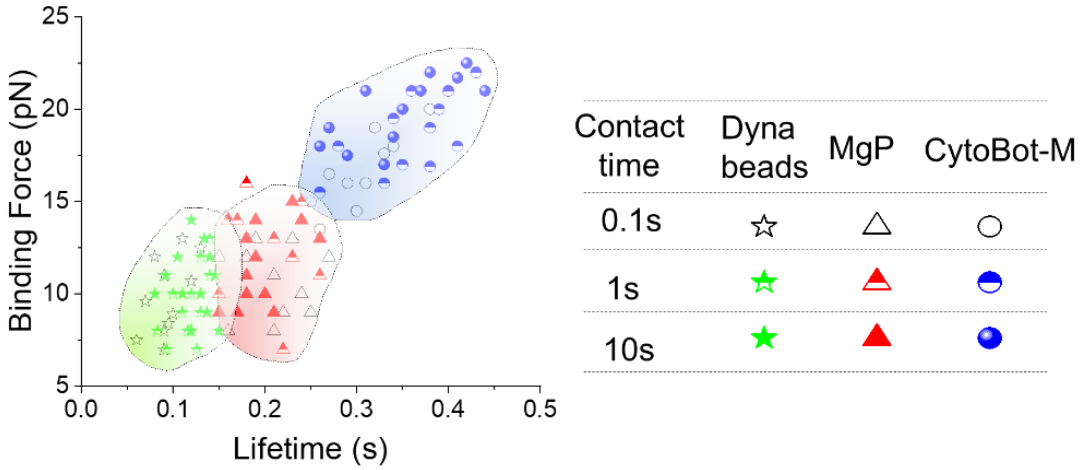


Figure S24. Quantitative analysis of the relationship between binding force and bond lifetime as contact time increases.

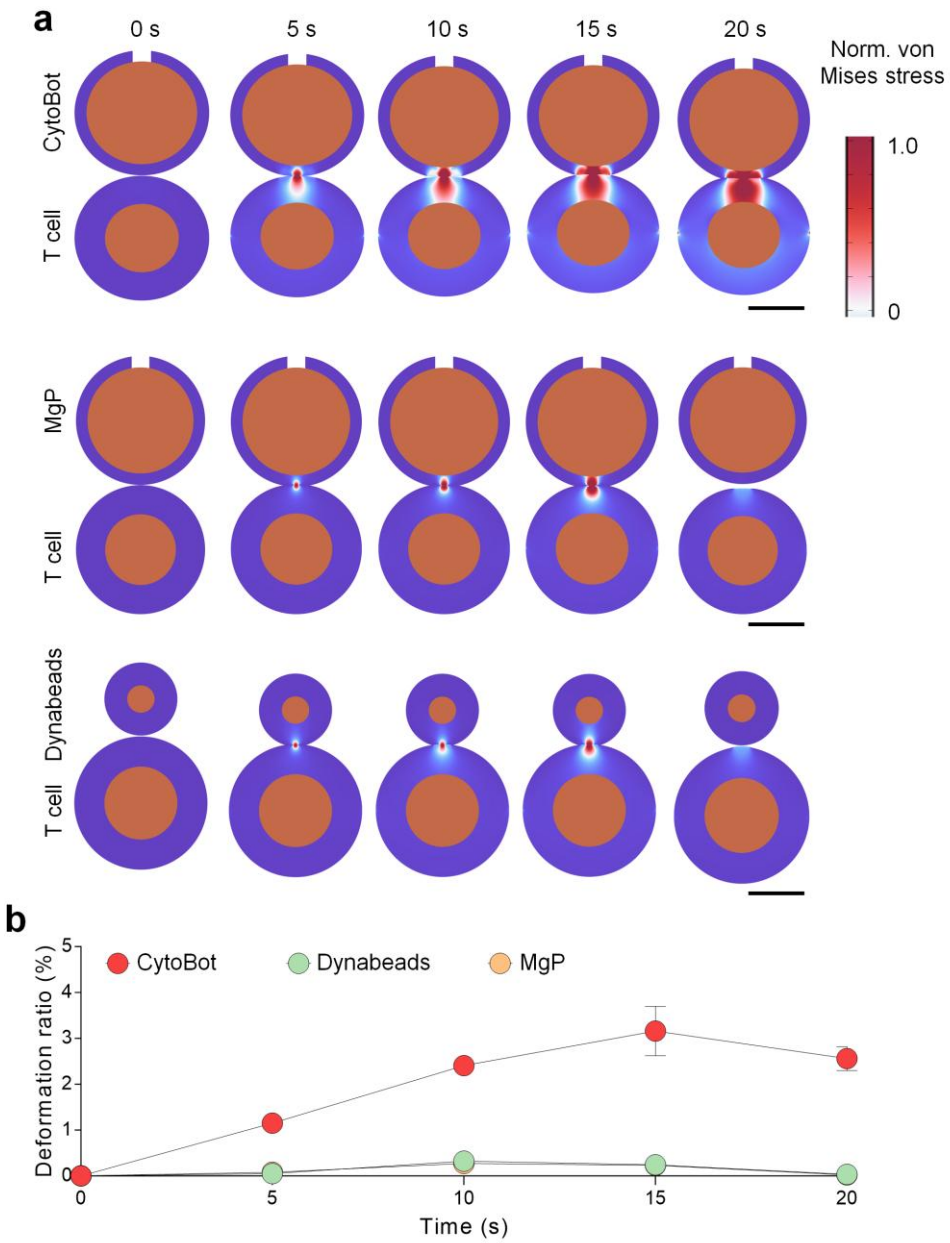


Figure S25. Mechanical interactions of Cytobot with T cell. Finite element simulations were performed by using COMSOL Multiphysics to estimate the time-dependent mechanical interactions between various microparticles and T cells. Representative time-dependent von Mises stress distributions illustrate the temporal change of localized mechanical stresses at the particle–cell interface.

(a) Finite element simulation of interactions of CytoBot, MgP or Dynabead with T Cell showing localized membrane deformation and confined stress zones at the interface with T-cell. Scale bar, 5 μm.

(b) Time-dependent T-cell deformation during interactions with Cytobot, Dynabeads, and MgP.

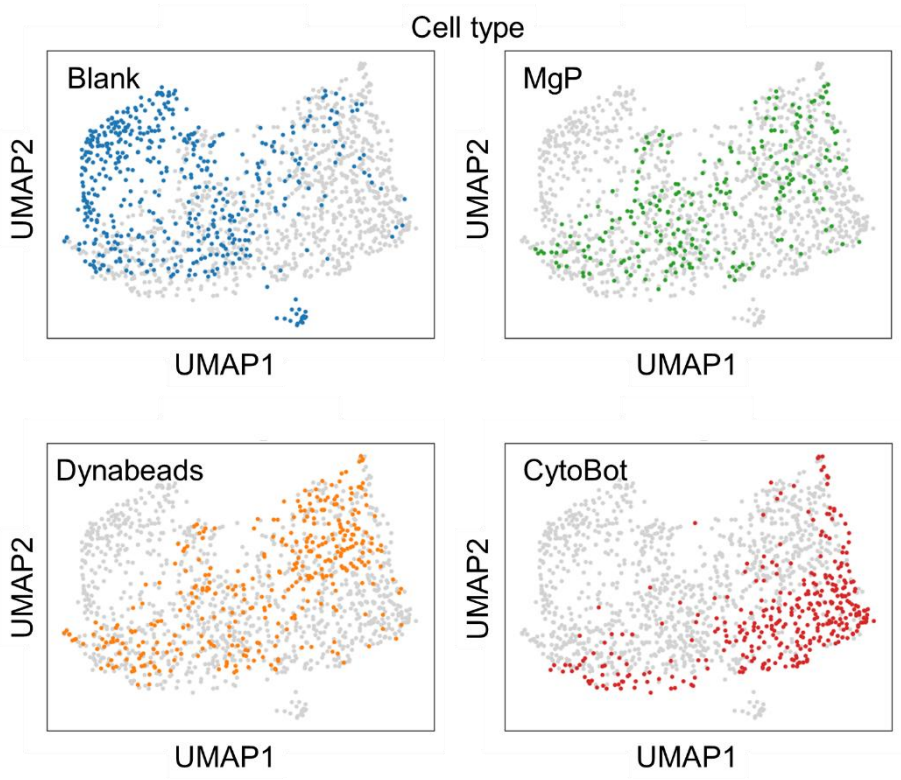


Figure S26. Uniform manifold approximation and projection (UMAP) analysis was performed to classify T cells based on key metabolic and morphological parameters extracted from FLIM measurements. UMAP visualization of cells under various conditions. Clear clustering is observed, with the Blank group located in the upper-left region and the CytoBot group in the lower-right region of the UMAP space. The MgP and Dynabead-treated groups also exhibit distinct shifts from the control group.

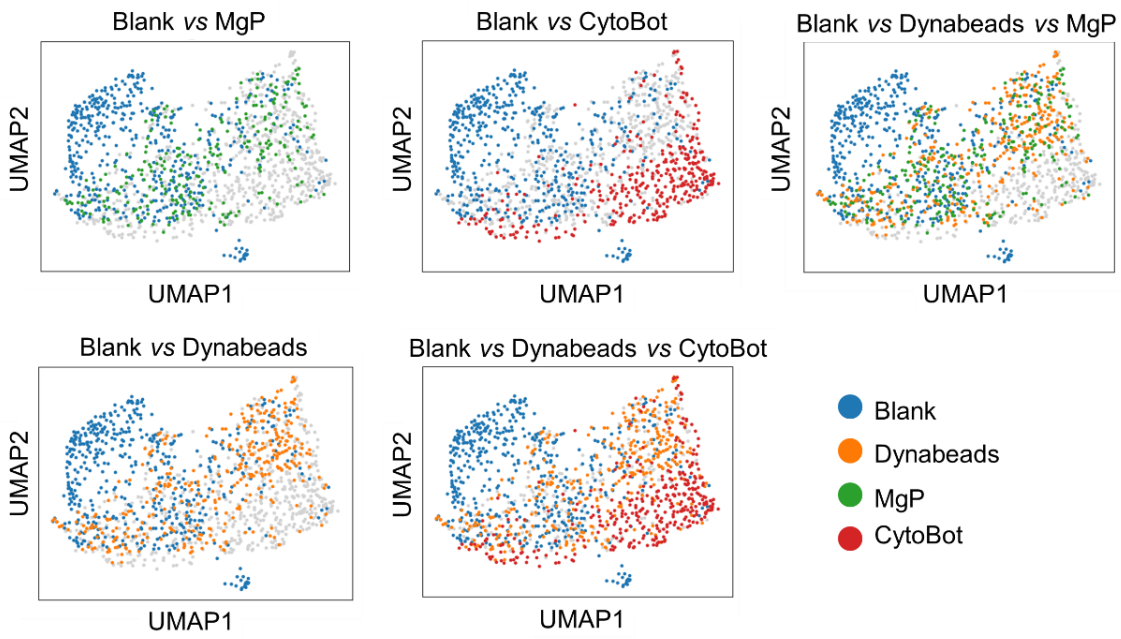


Figure S27. UMAP visualization of FLIM profiles of T cells under different stimulation conditions. Pairwise and combined UMAP projections showing the distribution of T cells from the Blank, MgP, Dynabeads, and CytoBot groups. Each dot represents an individual cell, colored according to its treatment group (Blank, blue; MgP, green; Dynabeads, orange; CytoBot, red). The plots illustrate the distribution and overlap of cells across treatment conditions in a shared FLIM-derived feature embedding.

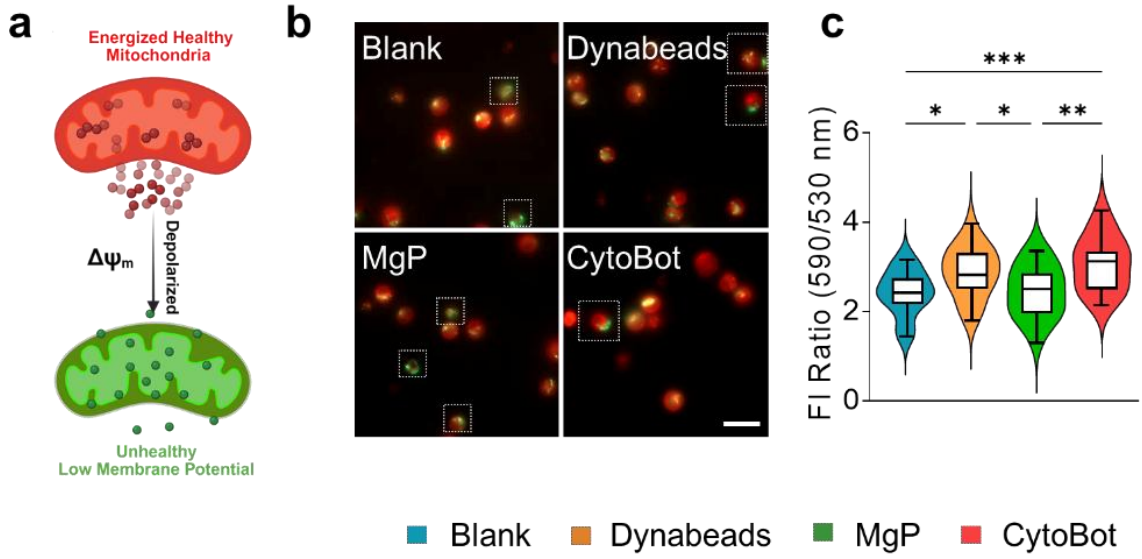


Figure S28. CytoBot stimulation enhances mitochondrial membrane potential in T cells.
(a) Schematic illustrating mitochondrial membrane potential: energized mitochondria with high membrane potential (Δψm) exhibit strong JC-1 aggregation–dependent red fluorescence, whereas depolarized, unhealthy mitochondria display diminished Δψm.
(b) Representative JC-1 staining images of T cells after stimulation by Blank, Dynabeads, MgPs , or CytoBots for day 2. CytoBot-treated cells exhibit the brightest red aggregates. Scale bar, 20 μm.
(c) Quantification of JC-1 aggregate/monomer fluorescence ratio (590/530 nm), showing significantly increased mitochondrial membrane potential in CytoBot-activated T cells compared with other groups.
Data are shown as mean ± SEM, n ≥ 6. Multiple comparisons were performed using one-way ANOVA, followed by Tukey's multiple comparisons test; **P* < 0.05, ***P* < 0.01, ****P* < 0.001, *****P* < 0.0001.

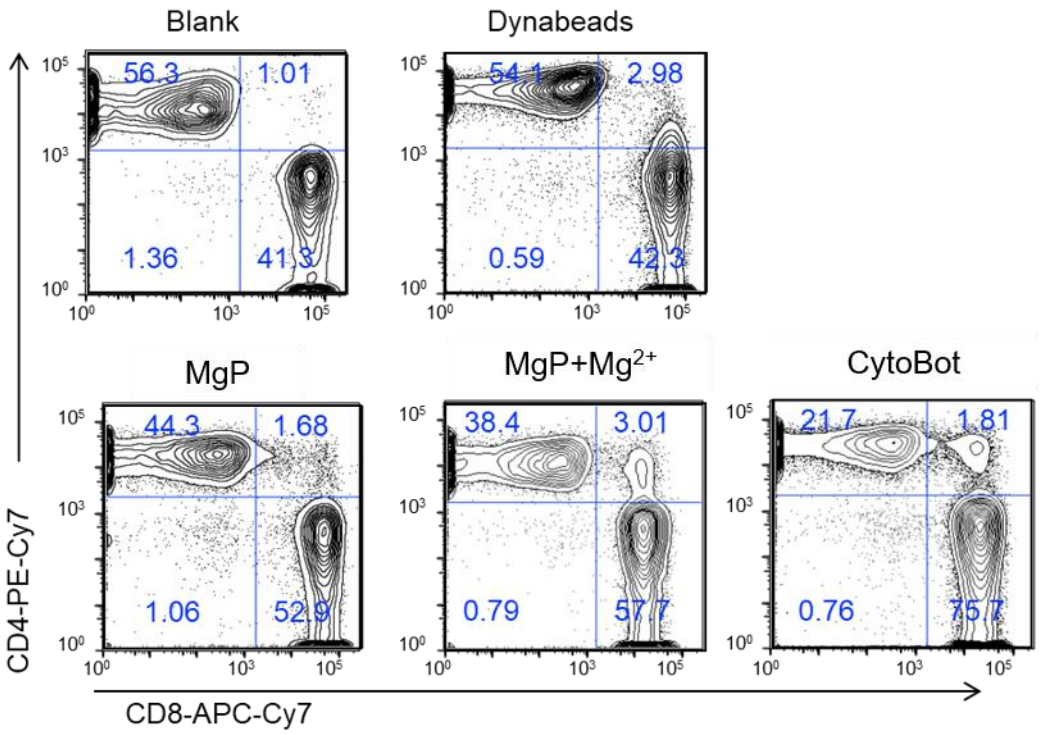


Figure S29. Flow cytometry of $CD4^+$ and $CD8^+$ T cell composition on Day 7 under different activation conditions (number of samples *n* =4).

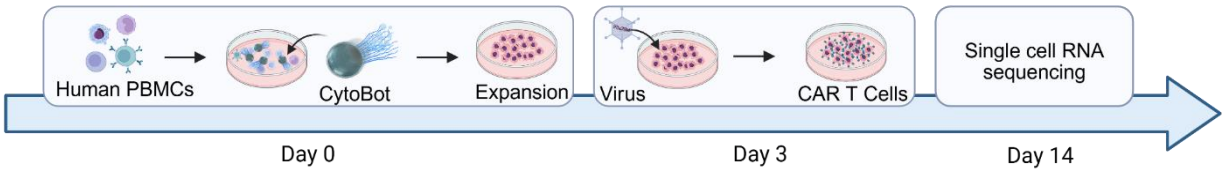


Figure S30. Schematic overview of the experimental design for single-cell RNA sequencing (scRNA-seq) of CAR-T cells activated with CytoBot, MgP, or Dynabeads.

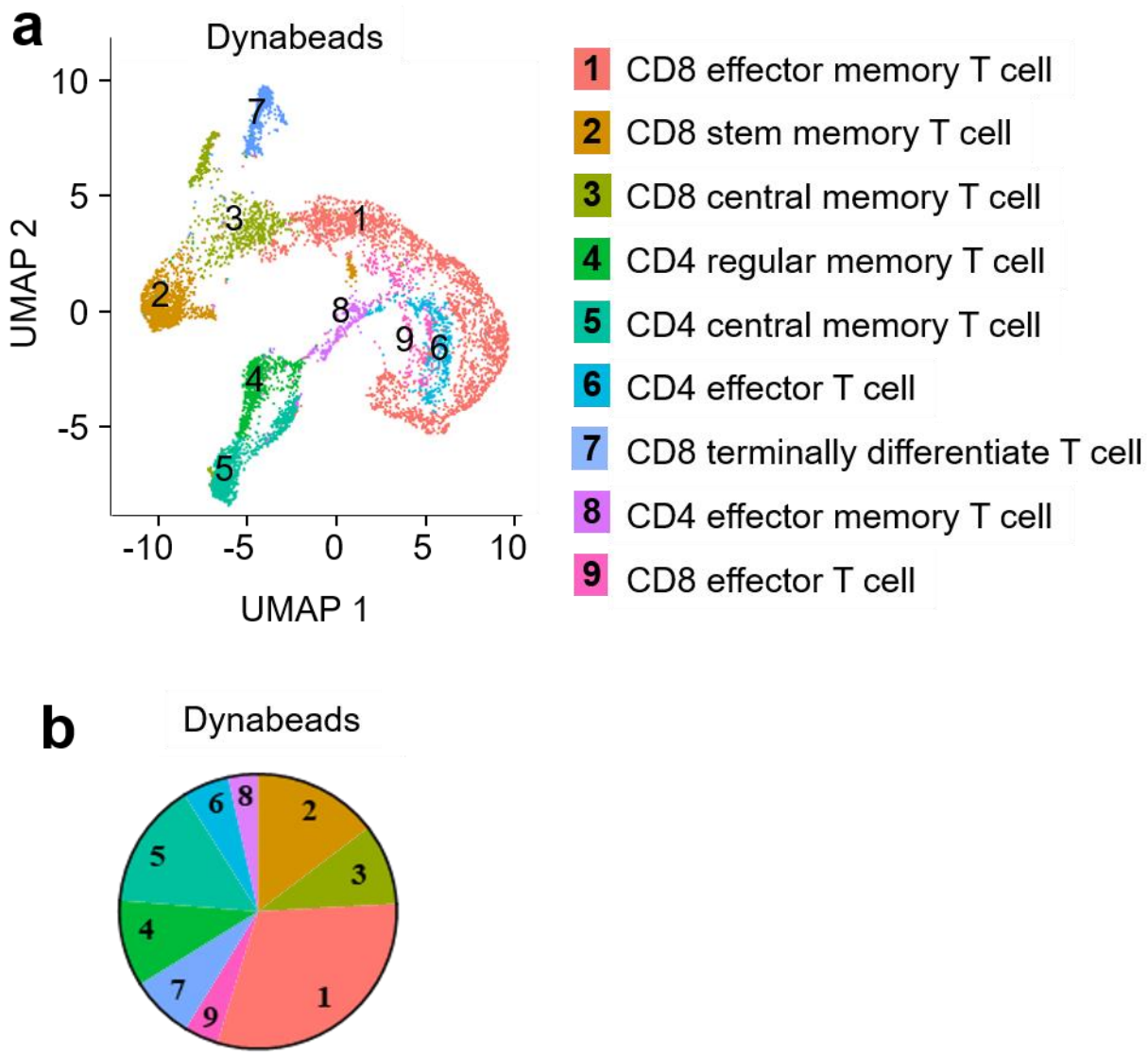


Figure S31. Single-cell transcriptomic profiling and T-cell subpopulation distribution in the Dynabeads group.

(a) UMAP projection of T cells (9,120 Dynabeads) identifying nine transcriptionally distinct clusters, including $CD8^+$ effector, stem-like, and central memory T cells; $CD4^+$ regulatory, central, and effector memory T cells; and terminally differentiated $CD8^+$ T cells.

(b) Pie chart illustrating the distribution of the 9 identified T-cell clusters in the Dynabeads group.

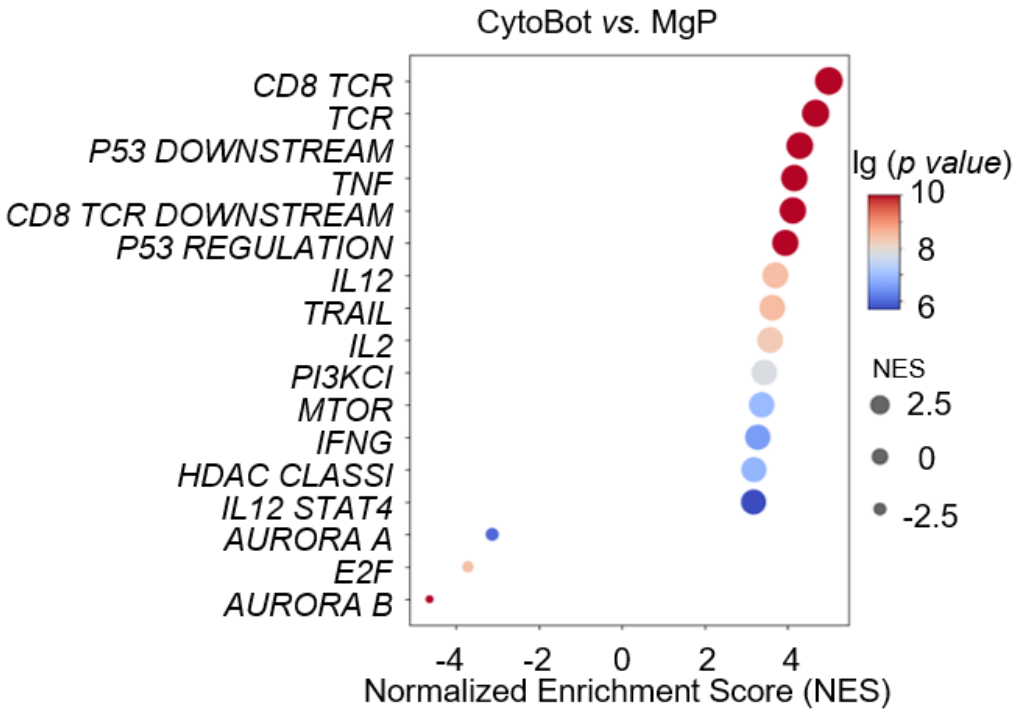


Figure S32. Gene set enrichment analysis of TCR-related, PI3K–mTOR-associated, and cytokine signaling pathways in CytoBot-expanded T cells compared with MgP controls.

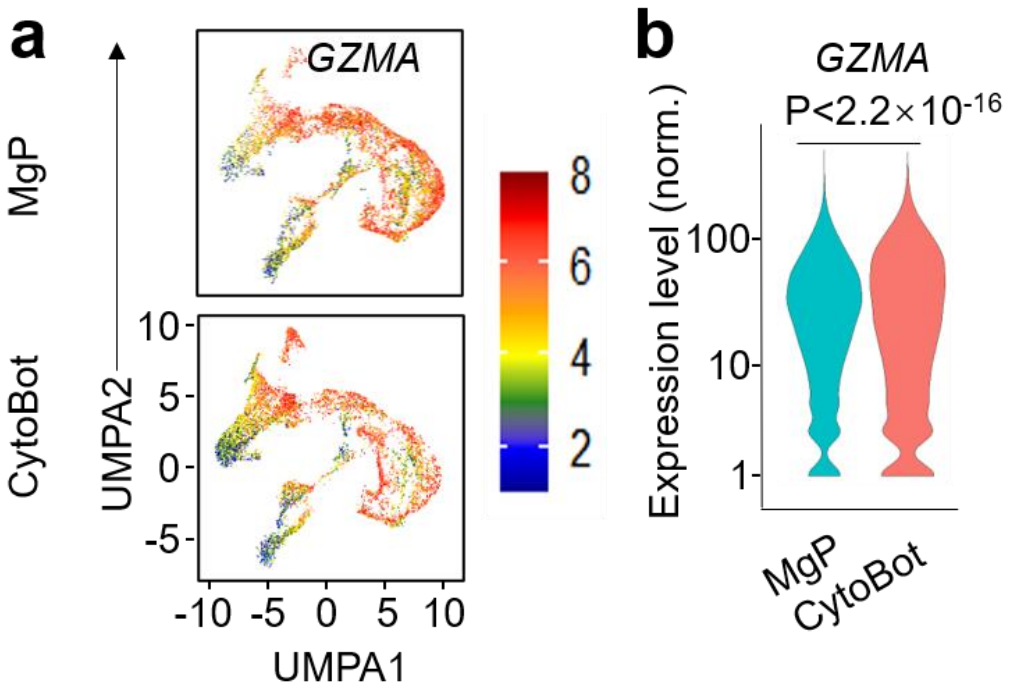


Figure S33. Single-cell transcriptomic analysis of GZMA expression in MgP- and CytoBot-expanded T cells.

(a) Representative feature plots showing the distribution of *GZMA* expression in MgP and CytoBot-expanded T cells.

(b) Violin plot showing the normalized expression of *GZMA* in MgP and CytoBot-expanded T cells. Statistical significance was determined using a two-sided Wilcoxon rank-sum test.

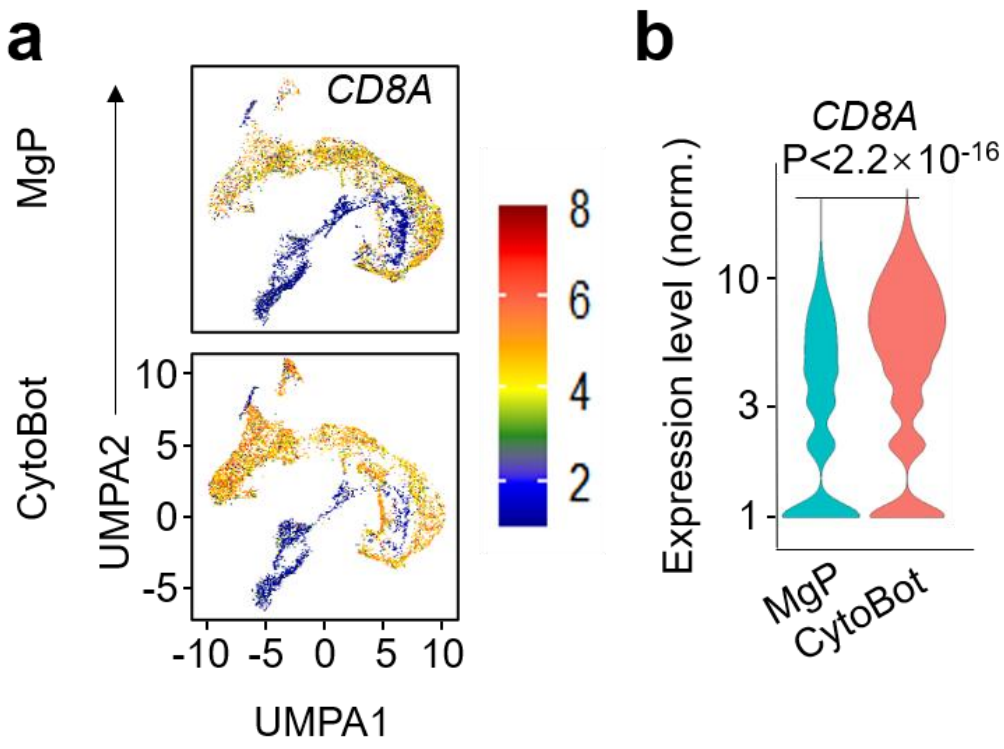


Figure S34. Single-cell transcriptomic analysis of CD8A expression in MgP- and CytoBot-expanded T cells.

(a) Representative feature plots showing the distribution of *CD8A* expression in MgP and CytoBot-expanded T cells.

(b) Violin plot showing the normalized expression of *CD8A* in MgP and CytoBot-expanded T cells. Statistical significance was determined using a two-sided Wilcoxon rank-sum test.

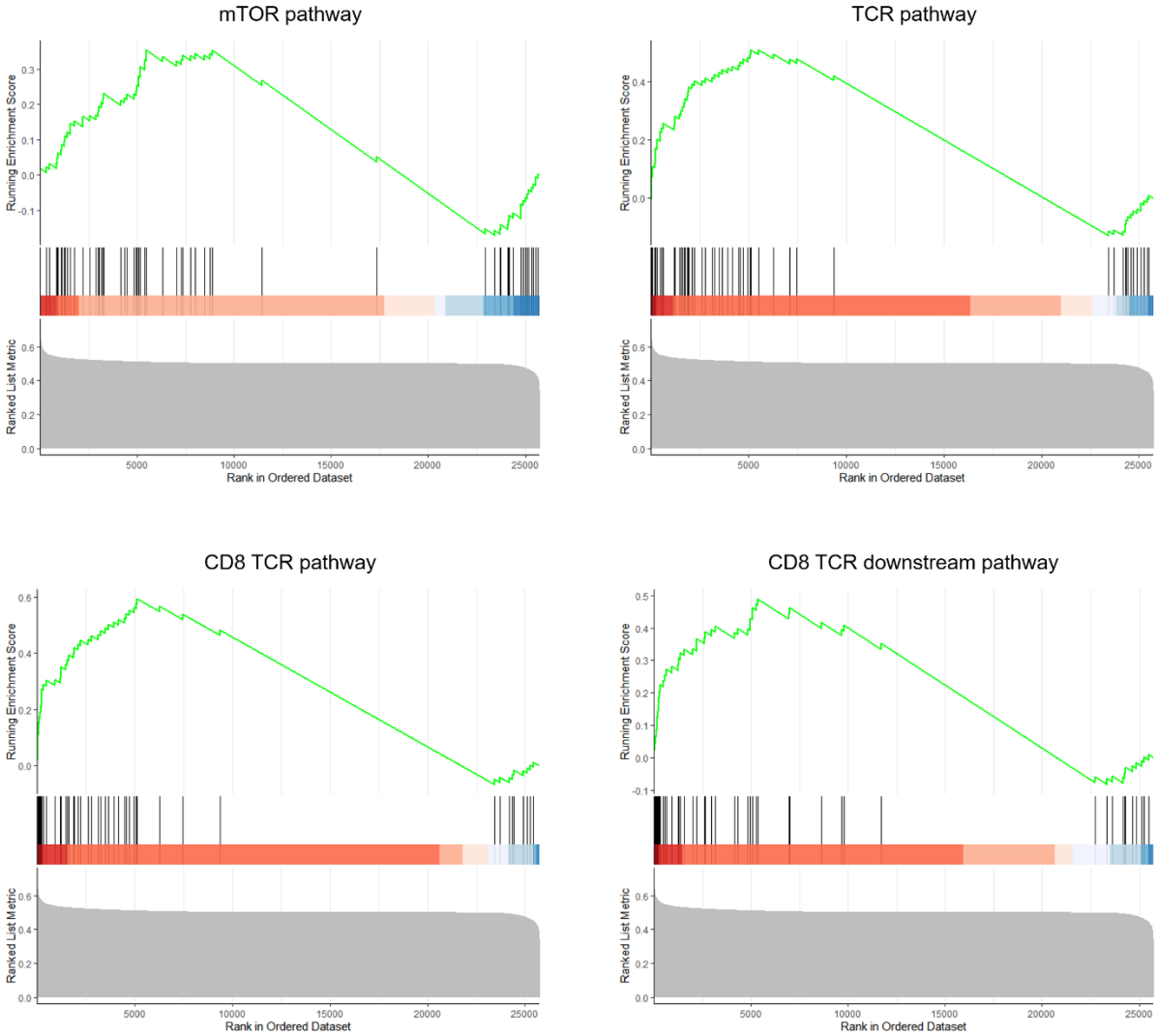


Figure S35. Gene set enrichment analysis (GSEA) showing positive enrichment of the mTOR, TCR and CD8 TCR signaling pathways in CytoBot-expanded T cells compared with the MgP group.

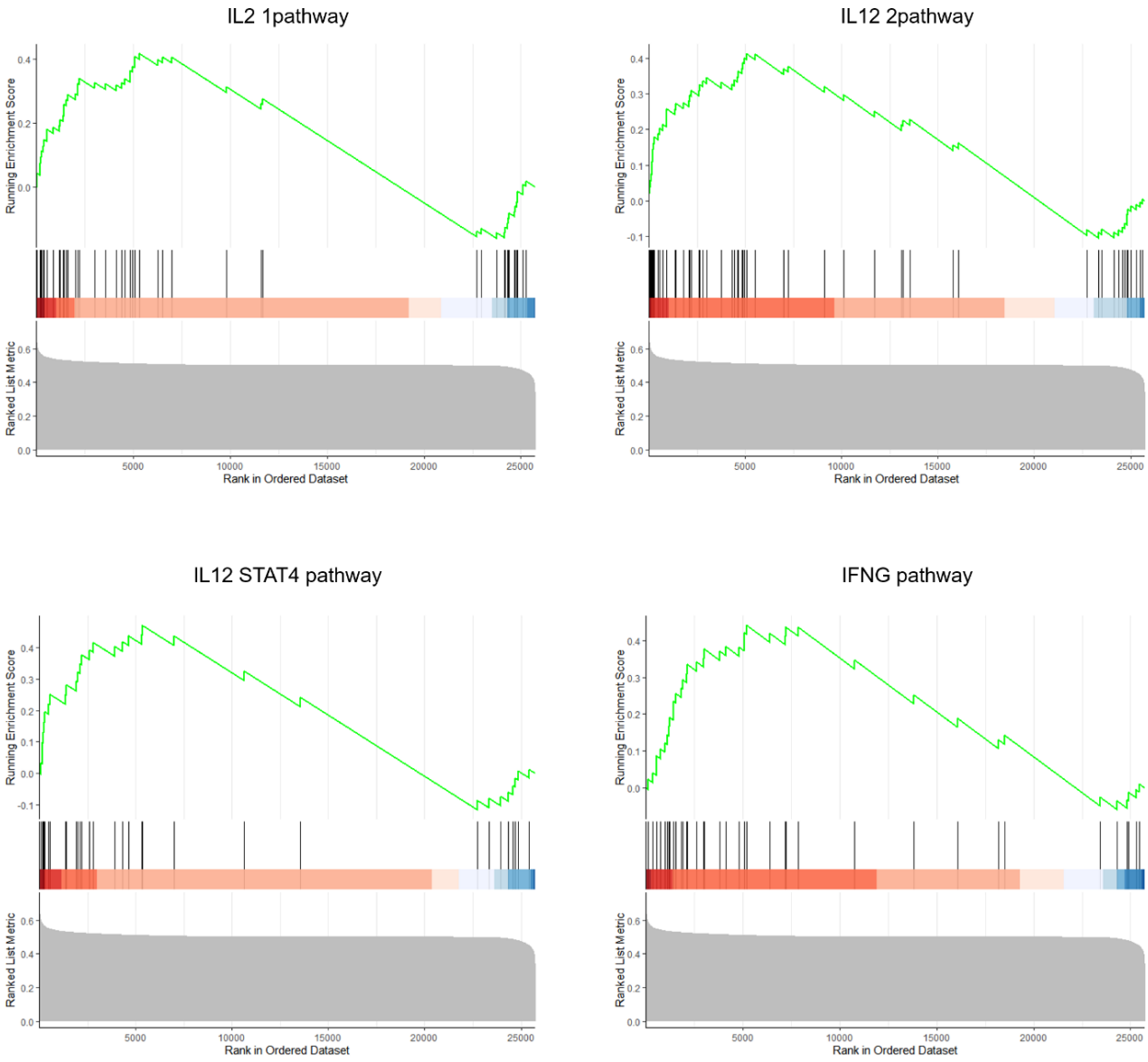


Figure S36. Gene set enrichment analysis (GSEA) showing positive enrichment of the IL2, IL12 and IFNG signaling pathways in CytoBot-expanded T cells compared with the MgP group.

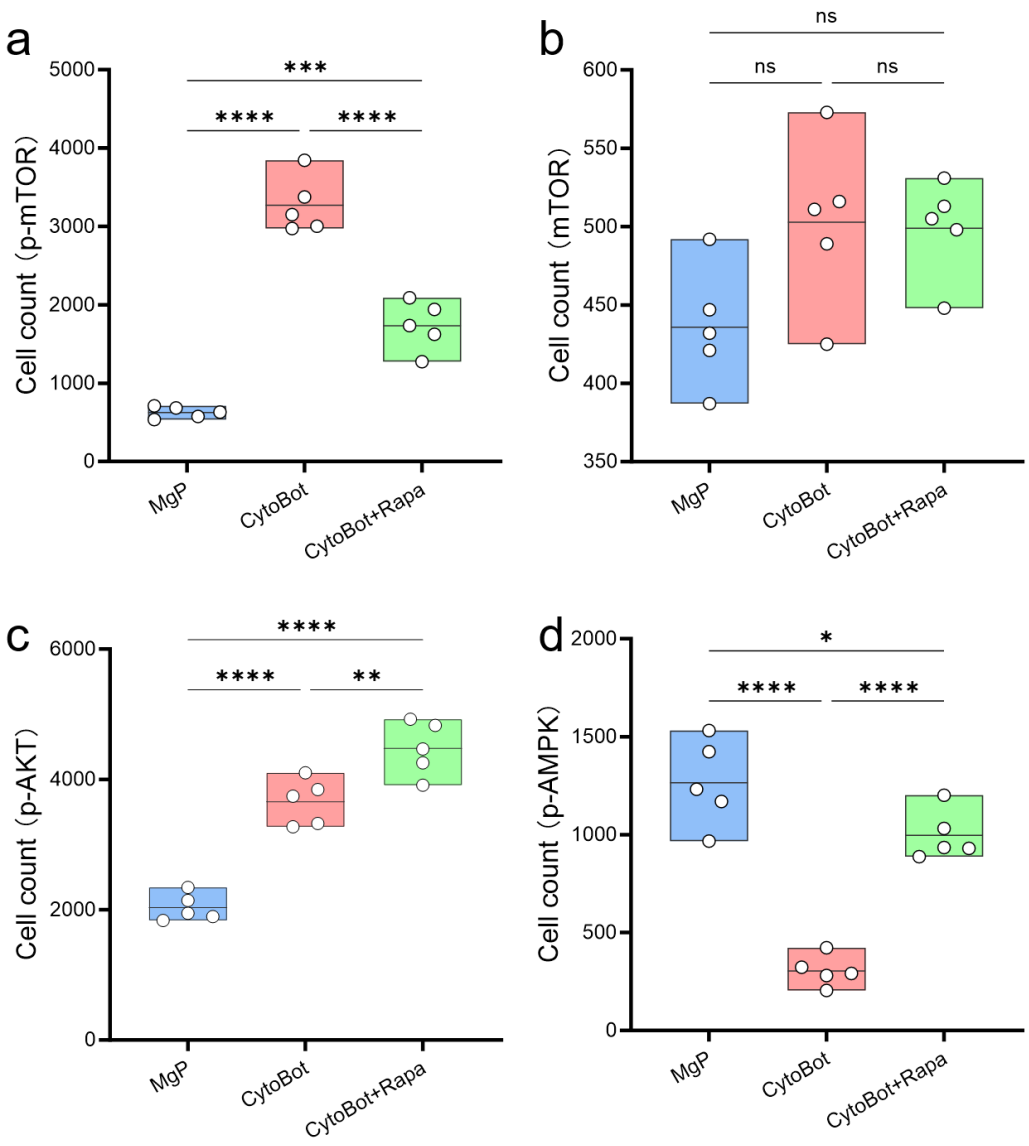


Figure S37. Quantification of PI3K–Akt–mTOR signaling activation in T cells following CytoBot stimulation.

(a) Quantification of phosphorylated mTOR (p-mTOR).

(b) Quantification of total mTOR expression.

(c) Quantification of phosphorylated AKT (p-AKT).

(d) Quantification of phosphorylated AMPK (p-AMPK) in T cells treated with MgP, CytoBot, or CytoBot plus rapamycin (Rapa).

Data are presented as box-and-whisker plots (center line, median; box, interquartile range; whiskers, min to max; dots represent individual biological replicates). Statistical significance was determined by one-way ANOVA with Tukey's multiple-comparisons test. *P < 0.05, **P < 0.01, ***P < 0.001, ****P < 0.0001; ns, not significant.

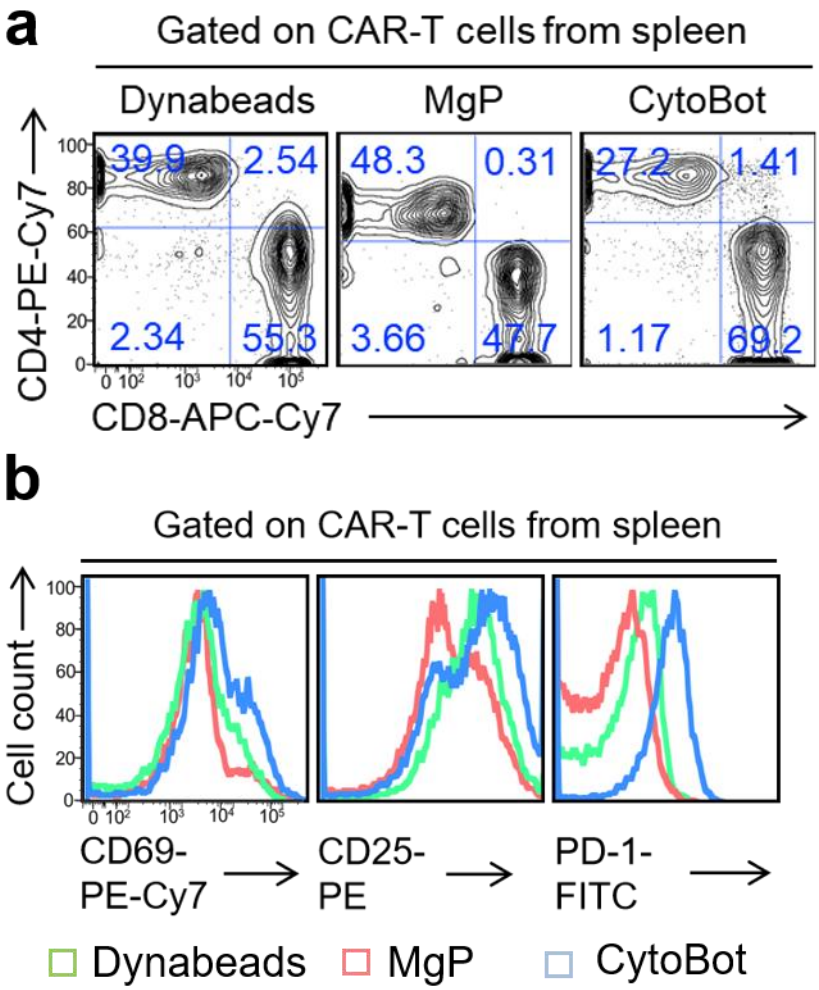


Figure S38. Long-term phenotypic characterization of splenic CAR-T cells and assessment of activation and exhaustion markers.

(**a**) Flow cytometric analysis of CD8/CD4 CAR-T cells in the spleen on day 80.

(**b**) Assessing expression of activation (CD69, CD25) and exhaustion (PD-1) markers (number of samples n = 5).

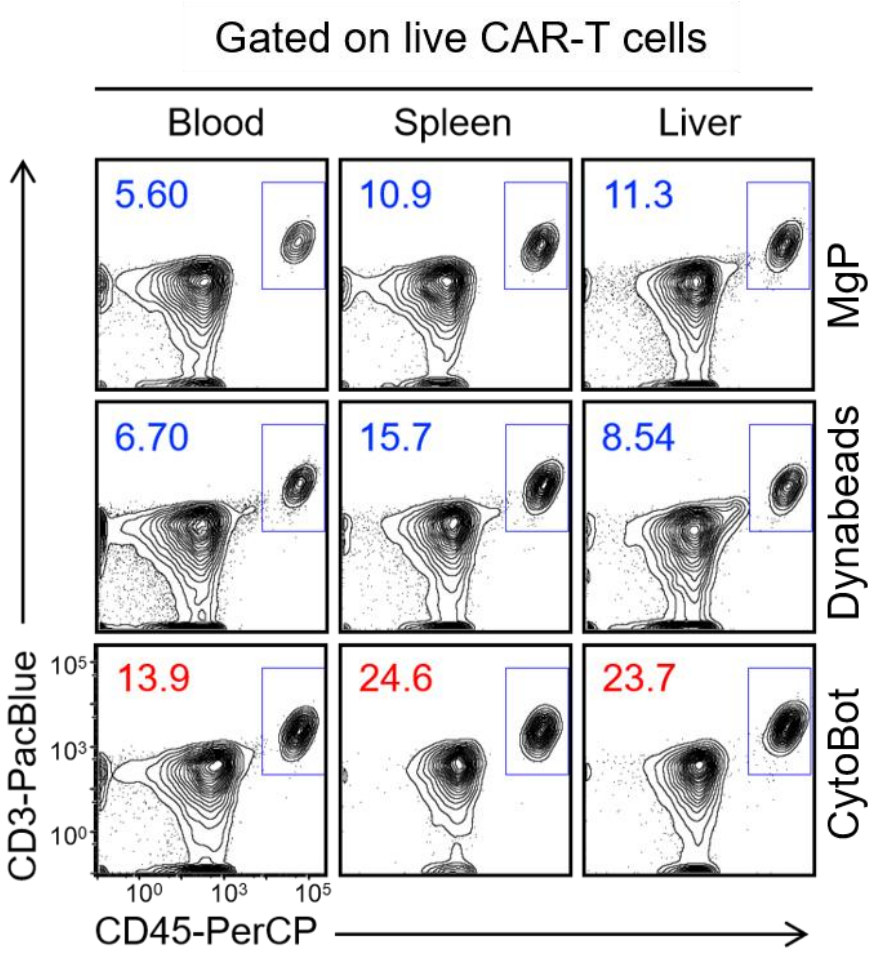


Figure S39. Flow cytometric analysis of CAR-T cells in mouse blood, spleen, and liver on day 80 (number of samples n = 5).

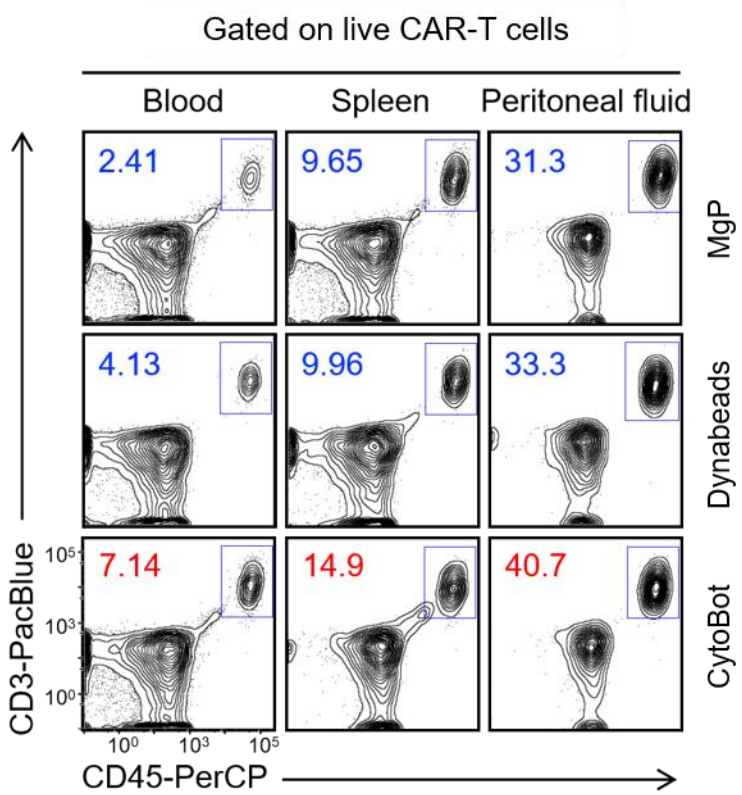


Figure S40. Flow cytometric analysis of CAR-T cells in mouse blood, spleen, and peritoneal fluid on day 51 (number of samples n = 5).